# Marsaalamite-(Y), Y(MoO₄)OH, a new molybdate mineral from the Um Safi area, Marsa Alam District, Central Eastern Desert of Egypt

**Nasser Mourad Mahdy[1,2]\*, Martin Ondrejka[2], Peter Bačík[2,3], Cristian Biagioni[4], Jiří Sejkora[5], Pavel Uher[2], Martin Števko[3,5], Hans-Jürgen Förster[6], Tomáš Mikuš[7]**

[1]Nuclear Materials Authority, P.O. 530, El-Maadi, Cairo, Egypt.
[2]Department of Mineralogy, Petrology and Economic Geology, Faculty of Natural Sciences, Comenius University, Mlynská dolina, Ilkovičova 6, 84215 Bratislava, Slovakia.
[3]Earth Science Institute, Slovak Academy of Sciences, Dúbravská cesta 9, 84005, Bratislava, Slovakia.
[4]Dipartimento di Scienze della Terra, Università di Pisa, Via Santa Maria, 53, I-56126 Pisa, Italy.
[5]Department of Mineralogy and Petrology, National Museum, Cirkusová 1740, 193 00 Prague 9, Czech Republic.
[6]GFZ Helmholtz Centre for Geosciences, D-14473 Potsdam, Germany.
[7]Earth Science Institute, Slovak Academy of Sciences, Ďumbierska 1, 97401, Banská Bystrica, Slovakia.

\*E-mail: nassermahdy91@yahoo.com.

## Abstract

Marsaalamite-(Y), ideally Y(MoO₄)OH, is a new molybdate mineral discovered in the greisenized Um Safi F-rich granite located in the Marsa Alam District, Central Eastern Desert of Egypt. It typically occurs as inclusions in or intergrowths with F-rich zinnwaldite. It forms micaceous aggregates, with sizes varying from 0.1 to 1 mm. Marsaalamite-(Y) is non-magnetic, white in color, and has an earthy lustre and white streak. It is brittle (3–4 Mohs) and has basal cleavages {001}. The calculated density is 4.90 g.cm⁻³ based on the empirical formula and unit-cell parameters refined from X-ray powder diffraction data. Marsaalamite-(Y) is associated with arsenopyrite, baryte, bastnäsite-(Ce), cassiterite, chernovite-(Y), columbite-(Fe), fluocerite-(Ce), fluorite, iron oxy-hydroxides, löllingite, molybdenite, monazite-(Ce), pyrite, quartz, rutile, thorite, wolframite, wulfenite, xenotime-(Y), and several unidentified phases. The empirical

formula is $(Y_{0.67}Er_{0.10}Dy_{0.08}Yb_{0.08}Ho_{0.02}Lu_{0.02}Tm_{0.02}Ca_{0.01})_{\Sigma 1.00} (Mo_{0.95}S_{0.03}As_{0.01}P_{0.01})_{\Sigma 1.00}$ $O_{4.00}[(OH)_{0.88}F_{0.11}Cl_{0.01}]_{\Sigma 1.00}$; the ideal end member formula is $Y(MoO_4)(OH)$. The presence of a hydroxyl group has been confirmed by Raman and infrared spectroscopy, and its concentration has been calculated from the stoichiometry. Marsaalamite-(Y) is the natural (OH)-dominant analogue of synthetic $Y(MoO_4)F$. It is monoclinic, space group $P2_1/c$, with unit-cell parameters $a = 5.1863(7)$ Å, $b = 12.3203(11)$ Å, $c = 6.6953(7)$ Å, $\beta = 114.173(8)°$, $V = 390.30(8)$ Å$^3$, and $Z = 4$. Extreme fractionation of the parental halogen-rich, A-type granitic magma triggered the greisenization of the granite. The marsaalamite-(Y) occurred simultaneously with or immediately after the crystallization of F-rich zinnwaldite based on the textural relationship. Therefore, the crystallization of marsaalamite-(Y) was most likely controlled by fluid-induced processes rather than magmatic conditions. The new mineral was approved by the Commission on New Minerals, Nomenclature and Classification of the International Mineralogical Association (CNMNC-IMA) (IMA 2024-050) and named after the Marsa Alam District, Al-Bahr Al-Ahmer Governorate, Egypt.

**Key words:** new mineral; marsaalamite-(Y); molybdate; zinnwaldite; greisenized granite; Central Eastern Desert; Egypt

## 1. Introduction

Molybdenum (Mo, $Z = 42$) is a transitional metal that bears the Neo-Latin name *molybdaenum*, which is derived from the Ancient Greek word "Μόλυβδος", meaning "lead". It is a multi-valent element whose partitioning behaviour depends on the redox state of its environment. Because the charge, size, and physical properties of Mo vary depending on its oxidation state, its redox sensitivity essentially controls its geochemical behaviour. Therefore, Mo geochemistry has become an effective tool for monitoring redox conditions in, i.e. ocean basins (Dahl *et al.,* 2011), early atmospheric oxygenation (Anbar *et al.,* 2007), and the impact of subducted sediments and fluids on arc magmas (Freymuth *et al.,* 2015).

Molybdenum can display the oxidation states 2+, 3+, 4+, 5+, and 6+. The latter occurs also in the oxyanion $(MoO_4)^{2-}$. Molybdenum is the essential constituent of 86

minerals currently accepted by the Commission on New Minerals, Nomenclature and Classification of the International Mineralogical Association (IMA-CNMNC), with *ca.* 20 of them contain the $(MoO_4)^{2-}$ oxyanion in their crystal structure (http://cnmnc.units.it/). The small Su Seinargiu prospect in Sardinia, Italy, is a natural laboratory for creation of Mo-bearing mineral species and probably one of the most significant locations for the study of the mineralogy of Mo in the world. More than sixty distinct mineral species have been discovered there, with the majority of them formed in response to the alteration for primary molybdenite ± bismuthinite ± bismuth assemblages (Bonaccorsi and Orlandi, 2020).

The Arabian Nubian Shield (ANS), representing a juvenile terrain (i.e. a mantle-derived crust) formed during the Pan-African Orogeny (950–550 Ma), is unique for its widespread occurrence of alkaline granites (Stoeser, 1986; El-Bialy *et al.,* 2020). Some of them are highly evolved and strongly fractionated granites and host economic rare metal deposits (Be, Nb, Ta, Zr, U, Th, Mo, Y, REE, W, and Sn) (Küster, 2009; Mahdy *et al.,* 2023 and references therein). Rare metal granite magmas were intensely affected by the circulation of magmatic–hydrothermal fluids during the ultimate stage of solidification. These magma–expelled fluids were occasionally mixed with meteoric waters (Mahdy *et al.,* 2015, 2020 and references therein). Fluid exsolution is associated with an exceptional increase of rare metals concentrations and promoted concurrently pervasive granite alteration, mineral-fluid interaction, and the onset mineral dissolution-reprecipitation processes (Abdalla, 2009; Abdelfadil *et al.,* 2022). Therefore, rare metal granites in the ANS can potentially become the source of rare and/or new mineral species. Surprisingly, only a single new mineral species has been recorded in such granites, hydroxyplumbopyrochlore, $(Pb_{1.5}\square_{0.5})Nb_2O_6(OH)$, discovered in the Jabal Sayid peralkaline granitic complex, Saudi Arabia (Li *et al.,* 2020).

In this paper, we provided the full description of a new mineral species associated with rare metal F-rich rhyolite-granite intrusions from the Um Safi area of Marsa Alam District, Central Eastern Desert of Egypt. Marsaalamite-(Y), phonetically [ˈmæɾsæˈʕælæm.aɪt], has the ideal formula $Y(MoO_4)(OH)$ and is named after the area where the mineral was discovered, the Marsa Alam District (i.e. urban and rural parts),

Al-Bahr Al-Ahmer Governorate, Egypt. The mineral name includes the Levinson suffix (Y) to indicate the dominance of yttrium over the other lanthanides, in agreement with the nomenclature of REE mineral species (Bayliss and Levinson, 1988). Although hydroxyl REE molybdates are uncommon in nature, they have attracted considerable attention recently owing to their promising applications, especially in optics because framework structures of molybdates containing trivalent and rare earth ions can be attractive phosphorous-hosting materials (Dorzhieva et al., 2021).

The new mineral and its name have been approved by the IMA-CNMNC under the number 2024-050. The holotype specimen, represented by a one-inch polished section (NGH-1 sample), is deposited in the Museo di Storia Naturale dell'Università di Pisa, Via Roma 79, I-56011 Calci, Pisa, Italy, under the catalogue number 20074. A cotype specimen, also constituting a one-inch polished section (NGH-2B sample), is deposited the collection of the National History Museum, Vajanského nábrežie 2, P.O. BOX 13, 810 06 Bratislava, Slovak Republic, under the catalogue number M-20414.

## 2. Occurrence

Marsaalamite-(Y) was discovered in the highly evolved (F-rich) greisenized, A-type granite of the Um Safi area of Marsa Alam District, Central Eastern Desert (CED), Egypt. The CED is the central segment of the Eastern Desert of Egypt that represents the northern segment of the ANS (Fig. 1a; Johnson et al., 2011). The ANS is primarily composed of juvenile continental crust, which originated during the amalgamation of Gondwana, and represents the northern segment of the East African Orogen (EAO) (Johnson and Woldehaimanot, 2003). The rock exposures of the ANS in Egypt encompass two segments, the Eastern Desert and Sinai (Fig. 1a). The Eastern Desert of Egypt is tectonically divided into three parts (Stern and Hedge, 1985) based on the lithology, deformation, and igneous activity: Northern Eastern Desert (NED), Central Eastern Desert (CED), and Southern Eastern Desert (SED). The CED is typically known for the occurrence of numerous highly evolved rare metal granites (rich in Ta, Nb, Be, Sn, Zr, Th, Y, Th, U, W, Mo, and REE) (Mahdy et al., 2020, 2023).

The Um Safi area is bounded by latitudes 25° 20' 10"–25° 19' 25" N and longitudes 34° 7' 40"–34° 8' 40" E. The exposed country rocks of the granites include mainly serpentinites and related talc-carbonate rocks, and island-arc volcanic assemblages, such as meta-andesites, volcanoclastic and volcano-sedimentary rocks (Fig. 1b). Serpentinites are the most distinctive lithological units and essential component in ophiolitic complexes of the ANS. Usually, the serpentinite blocks are altered to talc-carbonates, and the island arc rocks are commonly deformed, sheared, and metamorphosed up to the lower amphibolite facies. These metavolcanics in the Um Safi area are intruded by numerous sulfides-bearing quartz veins, striking predominantly NW–SE and NE–SW (Fig. 1b). Sulfur-bearing minerals occur as cavity fillings in these quartz veins and predominantly include galena and pyrite in addition to chrysocolla, anglesite, and atacamite as supergene products.

The Um Safi area contains two important types of magmatic rocks: F-rich granite (smaller exposure) and F-rich rhyolite (larger exposure). The area shows elliptical shape of 620 m × 450 m (Fig. 1b). The F-rich granite is intrusive into the rhyolite (Abdalla, 2001; Ibrahim, 2001). The marsaalamite-(Y)-bearing sample was collected from a granite exposure with the coordinates, latitude 25° 19' 51" N and longitude 34° 08' 13" E. The sampling location is intensively altered and sheared and shows intersection between rhyolite and granite with the talc serpentinite (Fig. 1b). As a result of hydrothermal alteration, it is difficult to distinguish granite from rhyolite in the field. These rhyolite and granite rocks extend NW–SE, compatible with the main trend of faults/shear zones associated with the Najd Fault System (NFS: NW-SE left-lateral strike-slip faults and shear zones). These NW–SE shear zones were active across the Precambrian of Arabia and Egypt (Fig. 1a) at 620–580 Ma during escape tectonics in the last phase of island arc accretion (shortening) caused by the Pan-African Orogeny, and acted as pathways for ascending rare metal, post-collisional granitic magmas (e.g. Mahdy et al., 2024). Therefore, the Um Safi F-rich rhyolite and associated F-rich granite may be genetically related, with the rhyolite representing the residual liquid of an associated, unexposed highly evolved rare metal granite magma.

The Um Safi F-rich granite is fine- to medium-grained and consists of feldspars, quartz, and biotite as essential mineralogical constituents. Greisenized domains within the granite are characterized by the hydrothermal alteration of feldspars into fine-grained muscovite, and of biotite into iron oxy-hydroxides and muscovite. This greisenized granite is rich in fluorite that occurs as disseminations or veinlets-filling fractures and is colorless to violet. Abundant hematitisation causes the dark pigmentation of the granitic rock. The Um Safi F-rich rhyolite is generally aphanitic and made of holocrystalline with subordinate glass. The highly altered zones of rhyolite are largely influenced by fluoritisation, hematitisation, sericitisation, silicification, and martitisation, i.e. magnetite oxidizes to hematite.

Marsaalamite-(Y) is mainly intergrown with zinnwaldite (polylithionite–siderophyllite solid solution; F = 4−6 wt.%), quartz, zircon (Fig. 2), and thorite. It is associated with arsenopyrite, As-rich thorite, baryte, bastnäsite-(Ce), cassiterite, chernovite-(Y), columbite-(Fe), fluocerite-(Ce), fluorite, iron oxy-hydroxides, löllingite, members of the hübnerite–ferberite series, members of xenotime-(Y)–thorite solid solutions, molybdenite, monazite-(Ce), pyrite, rutile, unidentified arsenates and As-bearing minerals, unidentified Th phosphate minerals, wulfenite, and Yb-rich xenotime-(Y).

## 3. Physical and optical properties

Marsaalamite-(Y) rarely crystalised as individual grains; instead, it typically occurs as inclusions in or intergrowths with zinnwaldite (Fig. 2). It forms mica-like crystals of 0.1 to 1 mm in size. Marsaalamite-(Y) is non-magnetic, white in color, and has an earthy lustre and white streak. It is brittle with hardness between mica and calcite (3−4 Mohs), with basal cleavage {001} and uneven micaceous fractures. The calculated density is 4.90 g.cm$^{-3}$, based on the empirical formula and unit-cell parameters refined from the X-ray powder diffraction data.

Marsaalamite-(Y) is opaque (Fig. 2a, b). In reflected light, it is greyish white and shows a distinct bireflectance, while its pleochroism and anisotropy are distinct with greyish white tints. Furthermore, no internal reflections are recognized. Reflectance

6

values (WTiC Zeiss 370), measured in air (microspectrophotometer MSP400 Tidas at Leica microscope, objective 50×, step-size 1 nm; National Museum, Prague, Czech Republic), are listed in Table 1 (COM standard wavelengths are given in bold), and are shown in Figure 3. The complete reflectance dataset of marsaalamite-(Y) is provided as electronic supplementary materials (ESM) – Table S1. The character of reflectance curves for marsaalamite-(Y) with distinct minima at 451, 521, and 656 nm is uncommon. The use of other objectives (20× and 100×) provided the same results. The reflectance curves of the WTiC standard and the associated thorite show a normal appearance, excluding that analytical shortcomings are responsible for these abnormal reflectance data.

## 4. Chemical composition

The chemical composition of marsaalamite-(Y) was determined in wavelength-dispersive (WDS) mode using a JEOL JXA-8530F electron microprobe at the Earth Science Institute, Slovak Academy of Sciences in Banská Bystrica, Slovakia. An accelerating voltage of 15 kV and a beam current of 20 nA were used. The spot beam diameter varied from 2 to 6 μm. Raw counts were converted to oxide wt.% using the ZAF matrix correction. Corrections of line interferences were performed applying the method by Åmli and Griffin (1975). The detection limit for all elements is typically on the order of 0.01 to 0.03 wt.%. The concentrations of Ti, U, Al, Mn, and LREE (La to Eu) are mostly below their detection limits. Analytical conditions are summarized in Table 2, while the chemical data are reported in Table 3. The presence of $(OH)^-$ has been confirmed by Raman and infrared spectrometry (see below), and its value has been calculated from the empirical formula assuming that (OH + F + Cl) site is completely filled, i.e. = 1 apfu.

Chemical analyses of marsaalamite-(Y) were conducted on both crystals of the holotype specimen (NGH-1) and cotype specimen (NGH-2B). The major components of marsaalamite-(Y) are Mo (46.47–48.49 wt.% $MoO_3$, 0.91–0.96 apfu Mo), Y (25.78–26.93 wt.% $Y_2O_3$, 0.64–0.68 apfu Y), and HREE, in particular Er>Yb>Dy (6.20–6.77 wt.% $Er_2O_3$, 0.09–0.10 apfu Er; 4.99–5.54 wt.% $Yb_2O_3$, 0.07–0.08 apfu Yb; 4.73–5.25 wt.% $Dy_2O_3$, 0.07–0.08 apfu Dy). The empirical formula calculated on the basis of two

7

cations and F+Cl+OH=1 is $(Y_{0.67}Er_{0.10}Dy_{0.08}Yb_{0.08}Ho_{0.02}Lu_{0.02}Tm_{0.02}Ca_{0.01})_{\Sigma1.00}$ $(Mo_{0.95}S_{0.03}As_{0.01}P_{0.01})_{\Sigma1.00} O_{4.00}[(OH)_{0.88}F_{0.11}Cl_{0.01}]_{\Sigma1.00}$, while the simplified formula is $(Y,Er,Dy,Yb)(MoO_4)(OH,F)$. The ideal formula is $Y(MoO_4)(OH)$, which requires (in wt.%) $Y_2O_3$ 42.46, $MoO_3$ 54.15, $H_2O$ 3.39, totalling to 100.

The studied crystals of marsaalamite-(Y) are chemically homogenous with no distinct variations. The chondrite-normalized patterns exhibit conspicuous HREE enrichments (Ho,Er,Tm,Yb,Lu; 14.30–16.39 wt.% $HREE_2O_3$), steep MREE (Gd,Tb,Dy; 5.07–5.85 wt.% $MREE_2O_3$), and negligible LREE (La,Ce,Pr,Nd). The REE patterns resemble those of common Y-dominated minerals.

## 5. Raman spectroscopy

The Raman spectra of marsaalamite-(Y) were collected in the range 50 to 4000 cm$^{-1}$ using a DXR-dispersive Raman Spectrometer (Thermo Scientific) mounted on a confocal Olympus microscope (National Museum, Prague, Czech Republic). The Raman signal was excited by an unpolarized red 633 nm He−Ne gas laser and detected by a CCD detector. The experimental parameters were 100× objective, 10 s exposure time, 100 exposures, 25 μm pinhole spectrograph aperture, 4 mW laser power level, and 400 lines/mm grating. The spectra were repeatedly acquired from different grains to obtain a representative spectrum with the best signal-to-noise ratio. The eventual thermal damage of the measured spot was excluded by visual inspection of the excited surface after measurement, by observation of possible decay of spectral features in the start of excitation and checking for thermal downshift of Raman lines. The instrument was set up by a software-controlled calibration procedure using multiple neon emission lines (wavelength calibration), multiple polystyrene Raman bands (laser-frequency calibration) and standardized white-light sources (intensity calibration). Spectral manipulations were performed using the Omnic 9 software (Thermo Scientific). The observed main bands are (in cm$^{-1}$): 3570, 977, 924, 837, 806, 757, 719, 670, 632, 605, 586, 524, 469, 444, 402, 343, 316, 296, 255, 239, 222, 191, 122, and 94.

The Raman spectrum of marsaalamite-(Y) in the full range is given in Figure 4. The rationale of its interpretation is based on the previous study of molybdates (Sejkora *et al.,*

2014, 2023 and references therein). A weak sharp band at 3570 cm$^{-1}$ is assigned to the OH stretching vibration of the hydrogen-bonded hydroxyl groups. According to the empirical relation between energy of vibration and the corresponding bond length, i.e. the correlation equation in the form $v(\text{cm}^{-1}) = 3592\text{-}304 \cdot \exp(\text{-}d(\text{O}\ldots\text{O})/0.1321)$ (Libowitzky, 1999), this wavenumber corresponds to O–H···O hydrogen-bond length 3.1 Å. A very strong band at 924 cm$^{-1}$ with shoulder at 977 cm$^{-1}$ is assigned to the $v_1$ $(\text{MoO}_4)^{2-}$ symmetric stretching vibration. The occurrence of two components of this vibration probably reflects different Mo−O lengths in the MoO$_4$ tetrahedra. Three medium bands at 837, 806, and 757 cm$^{-1}$ relate to $v_3$ triply degenerate antisymmetric stretching vibrations of the $(\text{MoO}_4)^{2-}$ group. The region of stretching vibrations of the MoO$_4$ group of marsaalamite–(Y) well corresponds to that of synthetic Y(MoO$_4$)F (Schleid *et al.,* 2008), with bands at 980(m), 943(vs), 866(m), 808(m) and 762(m) cm$^{-1}$. Weak bands at 402 and 343 cm$^{-1}$ and moderate ones at 316 and 296 cm$^{-1}$ are attributed to the $v_2$ doubly degenerate and $v_4$ triply degenerate bending vibrations of the $(\text{MoO}_4)^{2-}$ group. The series of weak bands in the range 720–440 cm$^{-1}$ is probably connected with vibrations of Y(+REE)-(OH) bonds. Weak and very weak Raman bands below 260 cm$^{-1}$ are associated with rotational or translational modes of the $(\text{MoO}_4)^{2-}$ group, as well as the lattice modes.

## 6. Infrared spectroscopy

The infrared vibrational spectrum of marsaalamite-(Y) was recorded by the reflection method on a Nicolet iN10 microspectrometer (Thermo Scientific) equipped with a nitrogen cooled MCT/A detector (Nicolet CZ s.r.o., Prague, Czech Republic). Spectra over the 670 to 4000 cm$^{-1}$ range were obtained from a sample area of $50 \times 50$ μm by the co-addition of 256 scans, with a resolution of 4 cm$^{-1}$. Gold mirror was used as reflection background. Spectra were co-added to improve the signal-to-noise ratio and were corrected using the Kramers−Kronig correction, to remove spectral distortions from diffuse reflectance measurements. Spectral manipulations were performed using the Omnic 9 software (Thermo Scientific).

The infrared spectrum of marsaalamite-(Y) in the full range is given in Figure 5. The main bands observed are (in cm$^{-1}$): 3571, 1038, 971, 929, 845, 803, 727, and 697. A strong sharp band at 3571 cm$^{-1}$ is assigned to the $\nu$ (OH) stretching vibrations of the hydrogen-bonded hydroxyl groups; its wavenumber well matches that of the corresponding Raman band (3570 cm$^{-1}$). Moderate bands at 971 and 929 cm$^{-1}$ are attributed to the $\nu_1$ $(MoO_4)^{2-}$ symmetric stretching vibration. The strong band at 845 cm$^{-1}$ and the medium band at 803 cm$^{-1}$ are assigned to the $\nu_3$ triply degenerate antisymmetric stretching vibrations of the $(MoO_4)^{2-}$ group. Moderate bands at 727 and 697 cm$^{-1}$ are probably connected with vibrations of Y(+REE)–(OH) bonds.

## 7. Crystallography

A single-crystal X-ray diffraction study of marsaalamite-(Y) was impossible owing to the powder-like diffraction pattern of all checked grains, in agreement with the nature of the available material.

Owing to the small amount of pure material, X-ray powder diffraction data were collected using a Bruker D8 Venture single-crystal diffractometer equipped with a Photon III CCD area detector and microfocused CuK$\alpha$ radiation (The Centre for Instrument Sharing of the University of Pisa, Italy), simulating a Gandolfi-like geometry. Observed X-ray diffraction lines are reported in Table 4. Figure 6 shows the X-ray powder diffraction pattern, along with the position of diffraction lines in isotypic $Y(MoO_4)F$. Unit-cell parameters refined from the X-ray powder diffraction data in a monoclinic setting are, space group $P2_1/c$, $a = 5.1863(7)$ Å, $b = 12.3203(11)$ Å, $c = 6.6953(7)$ Å, $\beta = 114.173(8)°$, $V = 390.30(8)$ Å$^3$, and $Z = 4$.

The low concentration of F and the occurrence of O–H bonds, in accord with micro-Raman and infrared data, imply that marsaalamite-(Y) is the natural (OH)–analogue of synthetic $Y(MoO_4)F$ and $Y(MoO_4)Cl$ (Schleid *et al.,* 2008). $Y(MoO_4)F$ crystallizes in a primitive cell setting with space group $P2_1/c$, whereas the lattice of $Y(MoO_4)Cl$ is face-centred with space group $C2/m$. Both structures contain unique crystallographic sites with $Y^{3+}$ cations, which have a coordination environment of six $O^{2-}$ and two F$^-$ or Cl$^-$ anions. In $Y(MoO_4)F$, the coordination environment is a square antiprism, and for $Y(MoO_4)Cl$, a

trigon-dodecahedra coordinates $Y^{3+}$. The tetrahedral $(MoO_4)^{2-}$ units of the F-compound are bound through corner-sharing to six Y-centred polyhedra, whereas those of the Cl-bearing compound are bonded to five Y-centred polyhedral, both through corner- and edge-sharing (Schleid *et al.,* 2008). The predicted structure of marsaalamite-(Y) derived from synthetic $Y(MoO_4)F$ is shown in Figure 7.

To distinguish between two possible unit-cell symmetries, unit-cell parameters were refined with the DiffracPlus TOPAS software using Le Bail fitting with solutions in the monoclinic and triclinic systems. The solution in the $P2_1/c$ space group was the eighth best (Goodness of Fit (GoF) = 6.55), but the seven solutions can be derived from the $P2_1/c$ space group by a reduction in symmetry ($P2$, $P2_1$) and had very similar calculated unit-cell parameters. The best solution in the face-centred space group $C2$ had a GoF of only 4.74, and no result was found in space group $C2/m$. Consequently, it is far more likely that the structure of marsaalamite-(Y) is more similar to $Y(MoO_4)F$ than to $Y(MoO_4)Cl$. This is further expected from the similarity of Y–O (2.31–2.45 Å) and Y–F (2.24–2.31 Å) bond lengths in $Y(MoO_4)F$. In contrast, Cl forms much longer bonds with Y (2.71–2.76 Å), causing a large distortion of $YO_6Cl_2$ polyhedra and a change in symmetry.

The Rietveld refinement of the powder XRD pattern using the structural model of synthetic $Y(MoO_4)F$ (Schleid *et al.,* 2008) provided very similar unit-cell parameters, but with one order of magnitude larger standard uncertainties and $R_{Bragg}$ of 99.86. The XRD pattern displays a quality insufficient for a Rietveld structural refinement. Consequently, we decided to use parameters with a smaller standard deviation obtained from Le Bail fitting in the $P2_1/c$ space group, with $R_{Bragg}$ = 3.894.

For the sake of comparison, the CIF file of the synthetic $Y(MoO_4)F$, is freely available on the Crystallography Open Database (COD, https://www.crystallography.net/cod/).

## 8. Discussion and conclusion

### 8.1. Origin of marsaalamite-(Y)

There is some evidence implying that marsaalamite-(Y) probably is a late-magmatic–early postmagmatic phase: (1) The Um Safi granite is a highly evolved, volatile-rich igneous system high in REE, Th, Nb, Y, Mo, and As. (2) Marsaalamite-(Y) occurs as inclusions in or intergrows with the F-rich zinnwaldite and is associated with zircon and thorite. (3) Crystallization of F-rich zinnwaldite indicates increasing of oxygen fugacity, fluorine, and water in the environment of its formation during late-magmatic stage, and suggests extreme fractionation of the parent aqueous silicate magma, which means that the marsaalamite-(Y) may be formed during transitional magmatic–hydrothermal stage.

Like the greisenized Um Safi granite, F-rich zinnwaldite is abundant, for example, in greisenized granites and the greisen-type Sn–W–Li mineralization from Cínovec/Zinnwald, Czech Republic/Germany (e.g. Webster *et al.,* 2004; Breiter *et al.,* 2017), or in Neogene rhyolite on the Chios Island, Greece (Mitropoulos *et al.,* 1999). The exsolution of F-, Li-, and (OH)-rich mineralizing hydrothermal fluids in the course of differentiation of the parental halogen-rich granitic magma triggered the greisenization of the granite and the alteration of primary magmatic minerals. However, marsaalamite-(Y), which is intimately related to the F-rich zinnwaldite, is a mineral with OH>F, although the late exsolved mineralizing fluids in the Um Safi granite were rich in F and Li.

Marsaalamite-(Y) has frequently overgrown the rim of zinnwaldite in the greisenized Um Safi granite (Fig. 2). This indicates that the marsaalamite-(Y) was formed after most of the F became already fixed in the zinnwaldite and other F-rich mineral phases [e.g. bastnäsite-(Ce), fluorite, and fluocerite-(Ce)]. Furthermore, occurrence of marsaalamite-(Y) as inclusions in and overgrowths on the zinnwaldite suggests that marsaalamite-(Y) occurred simultaneously with or immediately after the crystallization of zinnwaldite. As a result, the formation of marsaalamite (Y) was most likely controlled by fluid-induced processes rather than magmatic conditions.

## 8.2. Relationships to other mineral species and synthetic materials

Marsaalamite-(Y) is a member of the Nickel & Strunz subgroup 7.GB (molybdates, wolframates, and niobates) with additional $H_2O$ and/or OH and the Dana subgroup 49.3

(hydrated molybdates and tungstates containing hydroxyl or halogen). It has a novel composition, and it does not correspond to any unnamed mineral species.

Among all known mineral species, more than 80 have molybdenum as an essential component. From these, only one has additionally REE as an essential component, the chemically and structurally distinct cubic tancaite-(Ce) from Su Seinargiu, Sarroch Sardinia, Italy, ideally $Fe^{3+}Ce^{3+}(MoO_4)_3 \cdot 3H_2O$ (Bonaccorsi and Orlandi, 2020). In contrast, marsaalamite-(Y) is related to the crystal structure of the halide derivatives of yttrium ortho-oxomolybdate, $Y(MoO_4)F$ and $Y(MoO_4)Cl$ (Schleid *et al.,* 2008). It is the natural (OH)–analogue of synthetic $Y(MoO_4)F$ as discussed previously. Table 5 compares these four species.

Marsaalamite-(Y) is the third mineral with type locality in Egypt after grandfathered mineral chalconatronite ($Na_2Cu(CO_3)_2 \cdot 3H_2O$) (Frondel and Gettens, 1955) and bahariyaite ($KMnO_4$) approved by IMA (Helmy *et al.,* 2020). However, chalconatronite has been found among the corrosion products of three ancient bronze objects from Egypt, which are from the Saite-Ptolomaic Period (663-630 B.C.) and the late Coptic Period of Egypt (before the 8th century A.D.), while bahariyaite remains a highly doubtful natural occurrence and is quite possibly anthropogenic in origin.

## Acknowledgements

Supplementary material. The supplementary material for this article can be found at https:......

**Competing interests**

The authors declare none.

**References**

Abdalla H.M. (2001) Geochemistry and origin of rare metal mineralization of Um Safi felsite, central Eastern Desert, Egypt. *Egyptian Journal of Geology*, **45**, 131–149.

Abdalla H.M. (2009) Mineralogical and Geochemical Characterization of Beryl-Bearing Granitoids, Eastern Desert, Egypt: Metallogenic and Exploration Constraints. *Resource Geology*, **59**, 121–139.

Abdelfadil K.M., Mahdy N.M., Ondrejka M. and Putiš M. (2022) Mineral chemistry and monazite chemical Th–U–total Pb dating of the Wadi Muweilha muscovite pegmatite, Central Eastern Desert of Egypt: constraints on its origin and geodynamic evolution relative to the Arabian Nubian Shield. *International Journal of Earth Sciences*, **111**, 823–860.

Abouelnaga H.S., El-Shayeb H., Mahmoud T., Gaafar I. and Donia A.A. (2015) Ground geophysical survey for studying the potentiality of uranium mineralization in rhyolite zone—Um Safi area, Central Eastern Desert, Egypt. *Arabian Journal of Geosciences*, **8**, 6279–6303.

Åmli R. and Griffin W.L. (1975) Microprobe analysis of REE minerals using empirical correction factors. *American Mineralogist*, **60**, 599–606.

Anbar A.D., Duan Y., Lyons T.W., Arnold G.L., Kendall B., Creaser R.A., Kaufman A.J., Gordon G.W., Scott C., Garvin J. and Buick R. (2007) A whiff of oxygen before the great oxidation event?. *Science*, **317**, 1903–1906.

Bayliss P. and Levinson A.A. (1988) A system of nomenclature for rare-earth mineral species: revision and extension. *American Mineralogist*, **73**, 93–99.

Bonaccorsi E. and Orlandi P. (2020) Tancaite-(Ce), ideally $FeCe(MoO_4)_3 \cdot 3H_2O$: description and average crystal structure. *European Journal of Mineralogy*, **32**, 347–354.

Breiter K., Ďurišová J., Hrstka T., Korbelová Z., Vaňková M.H., Galiová M.V., Kanický V., Rambousek P., Knésl I., Dobeš P. and Dosbaba M. (2017) Assessment of magmatic vs. metasomatic processes in rare-metal granites: a case study of the Cínovec/Zinnwald Sn–W–Li deposit, Central Europe. *Lithos*, **292**, 198–217.

Dahl T.W., Canfield D.E., Rosing M.T., Frei R.E., Gordon G.W., Knoll A.H. and Anbar A.D. (2011) Molybdenum evidence for expansive sulfidic water masses in 750 Ma oceans. *Earth and Planetary Science Letters*, **311**, 264–274.

Dorzhieva S.G., Sofich D.O., Bazarov B.G., Shendrik R.Y. and Bazarova J.G. (2021) Optical properties of molybdates containing a combination of rare-earth elements. *Inorganic Materials*, **57**, 54–59.

El-Bialy M.Z., Eliwa H.A., Mahdy N.M., Murata M., El-Gameel K.H., Sehsah H., Omar M., Kato Y., Fujinaga K., Andresen A. and Thomsen T.B. (2020) U-Pb zircon geochronology and geochemical constraints on the Ediacaran continental arc and post-collision granites of Wadi Hawashiya, Northeastern Desert, Egypt: Insights into the ~600 Ma crust-forming event in the northernmost part of Arabian-Nubian Shield. *Precambrian Research*, **345**, 105777.

Freymuth H., Vils F., Willbold M., Taylor R. and Elliot T. (2015) Molybdenum mobility and isotopic fractionation during subduction at the Mariana arc. *Earth and Planetary Science Letters*, **432**, 176–186.

Frondel C. and Gettens R.J. (1955) Chalconatronite, a new mineral from Egypt. *Science*, **122**, 75–76.

Helmy H.M., Euler H.J., Tomaschek F., Ballhaus C. and Friedrich H.H. (2020) Bahariyaite, IMA 2020-022. CNMNC Newsletter No. 57. *Mineralogical Magazine*, **84**. https://doi.org/10.1180/mgm.2020.73.

Ibrahim I.H. (2001) Geology, geochemistry and potentiality of radioactive mineralization at Um Safi area, Central Eastern Desert, Egypt. Ph.D. thesis, Faculty of Science, Ain Shams Univ. Cairo, Egypt, 268.

Johnson P.R. and Woldehaimanot B. (2003) Development of the Arabian-Nubian Shield: perspectives on accretion and deformation in the northern East African Orogen and the assembly of Gondwana. *Geological Society*, London, Special Publications, **206**, 289–325.

Johnson P.R., Andresen A., Collins A.S., Fowler A.R., Fritz H., Ghebreab W., Kusky T. and Stern R.J. (2011) Late Cryogenian–Ediacaran history of the Arabian–Nubian Shield: a review of depositional, plutonic, structural, and tectonic events in the closing stages of the northern East African Orogen. *Journal of African Earth Sciences*, **61(3)**, 167–232.

Küster D. (2009) Granitoid-hosted Ta mineralization in the Arabian–Nubian Shield: ore deposit types, tectono-metallogenetic setting and petrogenetic framework. *Ore Geology Reviews*, **35**, 68–86.

Li T., Li Z., Fan G., Fan H., Zhong J., Jahdali N.S., Qin M., Jehani A.M., Wang F. and Nahdi M.M. (2020) Hydroxyplumbopyrochlore, $(Pb_{1.5},\square_{0.5})\,Nb_2O_6\,(OH)$, a new member of the pyrochlore group from Jabal Sayid, Saudi Arabia. *Mineralogical Magazine*, **84**, 785–790.

Libowitzky E. (1999) Correlation of O-H stretching frequencies and O-H···O hydrogen bond lengths ln Minerals. *Monatshefte für Chemie*, **130**, 1047–1059.

Mahdy N.M., El Kalioubi B.A., Wohlgemuth-Ueberwasser C.C., Shalaby M.H. and El-Afandy A.H. (2015) Petrogenesis of U- and Mo-bearing A2- type granite of the Gattar batholith in the Arabian Nubian Shield, Northeastern Desert, Egypt: favorability of host rocks for the origin of associated ore deposits. *Ore Geology Reviews*, **71**, 57–81

Mahdy N.M., El-Arafy R.A., El-Qassas R.A., Metwaly M., Abd El-Rahman Y., El-Sundolly H.I. and Said A. (2024) Lithological discrimination of the Fawakhir-Atalla belt in the Central Eastern Desert of Egypt based on Landsat-9 remote sensing data, airborne gamma-ray spectrometry, field and petrographic investigations with implications on the evolution of the Arabian Nubian Shield. *Physics and Chemistry of the Earth*, Parts A/B/C, **134**, 103578.

Mahdy N.M., Iizuka T., Pease V., Ghoneim M.M. and Abdel–Hamid A.A.A. (2023) Origin, dynamics, and chemical evolution of garnet-bearing leucogranitic magma, Eastern Desert of Egypt: Controls on the rare-metal enrichment in the A-type magmatism. *Geochemistry*, **83**, 126025.

Mahdy N.M., Ntaflos T., Pease V., Sami M., Slobodník M., Abu Steet A.A., Abdelfadil K.M. and Fathy D. (2020) Combined zircon U-Pb dating and chemical Th–U–

total Pb chronology of monazite and thorite, Abu Diab A–type granite, Central
Eastern Desert of Egypt: constraints on the timing and magmatic-hydrothermal
evolution of rare-metal granitic magmatism in the Arabian Nubian Shield.
*Geochemistry*, **80**, 125669.

Mitropoulos P., Katerinopoulos A. and Kokkinakis A. (1999) Occurrence of primary
almandine–spessartine–rich garnet and zinnwaldite phenocrysts in a Neogene
rhyolite on the island of Chios, Aegean Sea, Greece. *Mineralogical Magazine*, **63**,
503–510.

Schleid T., Strobel S., Dorhout P.K., Nockemann P., Binnemans K. and Hartenbach I.
(2008) YF[MoO$_4$] and YCl[MoO$_4$]: Two halide derivatives of yttrium ortho–
oxomolybdate: Syntheses, structures, and luminescence properties. *Inorganic
Chemistry*, **47**, 3728–3735.

Sejkora J., Čejka J., Malíková R., López A., Xi Y. and Frost R.L. (2014) A Raman
spectroscopic study of a hydrated molybdate mineral ferrimolybdite,
Fe$_2$(MoO$_4$)$_3$·7−8 H$_2$O. *Spectrochimica Acta A*: Molecular and Biomolecular
Spectroscopy, **130**, 83–89.

Sejkora J., Pauliš P., Vrtiška V., Pour O. and Dvořák Z. (2023) Lindgrenite, monoclinic
Cu$_3$(MoO$_4$)(OH)$_2$, from Cínovec, Krušné hory Mountains - the first occurrence in
the Czech Republic. *Bulletin Mineralogie Petrologie*, **31**, 41–46.

Stern R.J. and Hedge C.E. (1985) Geochronologic and isotopic constraints on late
Precambrian crustal evolution in the Eastern Desert of Egypt. *American Journal
of Science*, **285**, 97–127.

Stoeser D.B. (1986) Distribution and tectonic setting of plutonic rocks of the Arabian
Shield. *Journal of African Earth Sciences*, **4**, 21–46.

Warr L.N. (2021) IMA-CNMNC approved mineral symbols. *Mineralogical Magazine*,
**85**, 291–320.

Webster J., Thomas R., Förster H.J., Seltmann R. and Tappen C. (2004) Geochemical
evolution of halogen-enriched granite magmas and mineralizing fluids of the
Zinnwald tin-tungsten mining district, Erzgebirge, Germany. *Mineralium
Deposita*, **39**, 452–472.

**Figure captions.**

**Figure 1:** (**a**) Geological map of the Eastern Desert and Sinai of Egypt as the northernmost part of the Arabian Nubian Shield (ANS) showing tectonic features, rock units, distribution of rare metal granites, and location of the Um Safi area (modified after Mahdy *et al.,* 2023). (**b**) Geological map of the Um Safi area showing the exposures of greisenized granite, F-rich rhyolite, and country rocks (modified after Abouelnaga *et al.,* 2015).
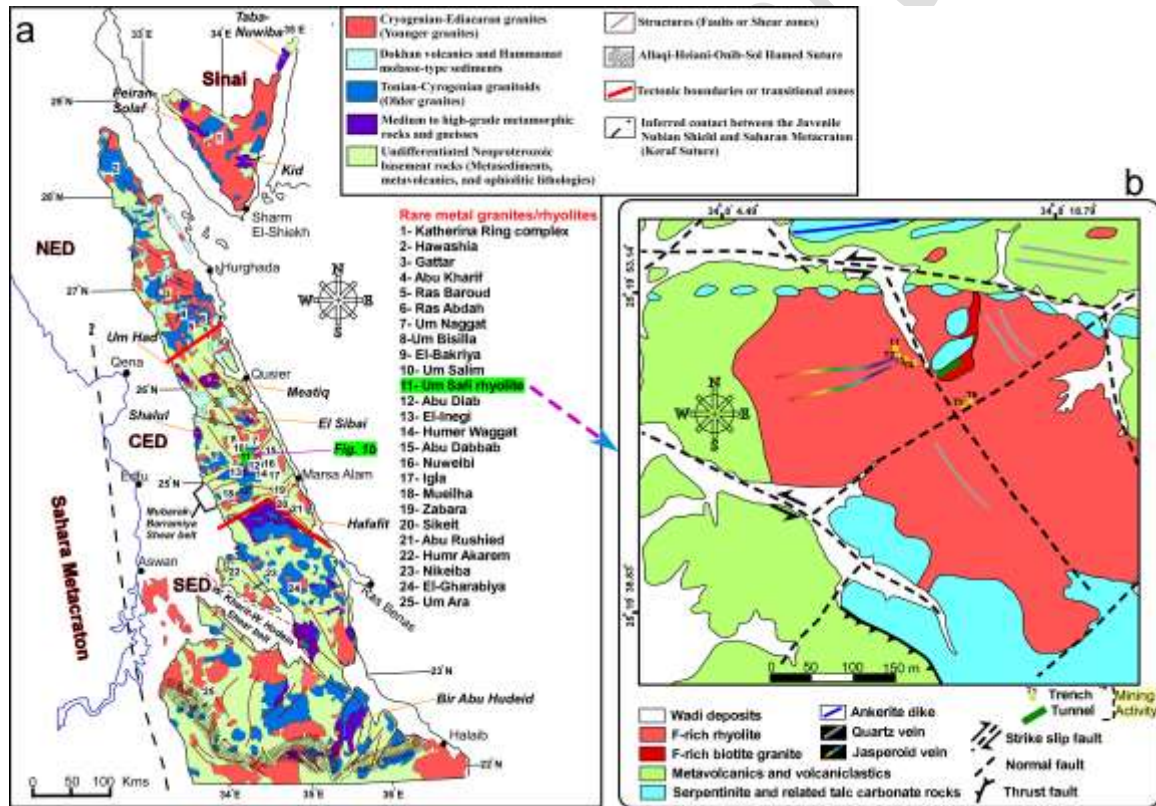
**Figure 2:** Optical and back-scattered electron (BSE) microphotographs of marsaalamite-(Y) (Maa-Y) and associated minerals (a) transmitted cross-polarized light (b) reflected plane-polarized light. (c) Maa-Y and zinnwaldide (Znw) intergrowths and intimately associated zircon (Zrn) and quartz (Qz). (**b**) Mica–like sheets of Maa-Y with perfect basal cleavages, similar to textural features of mica minerals and molybdenite. Mineral symbols are from Warr (2021).
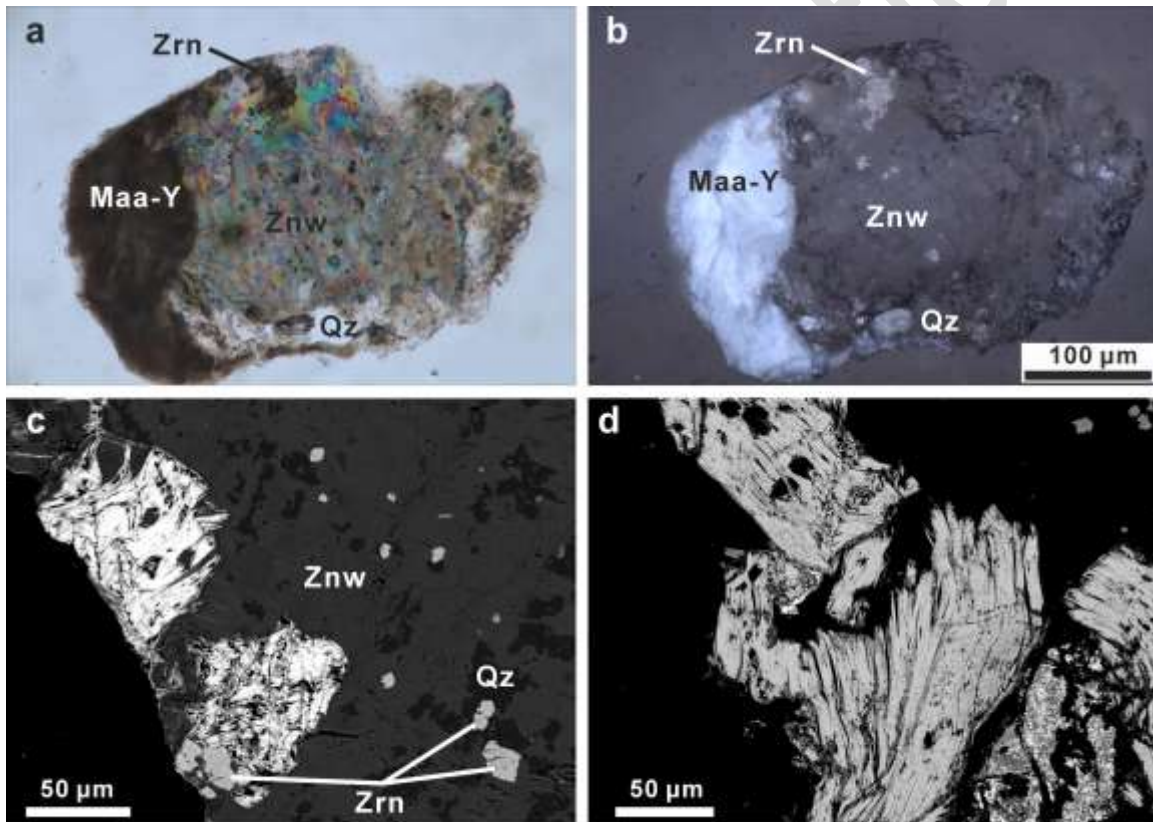
**Figure 3:** Reflectance curves for marsaalamite-(Y).
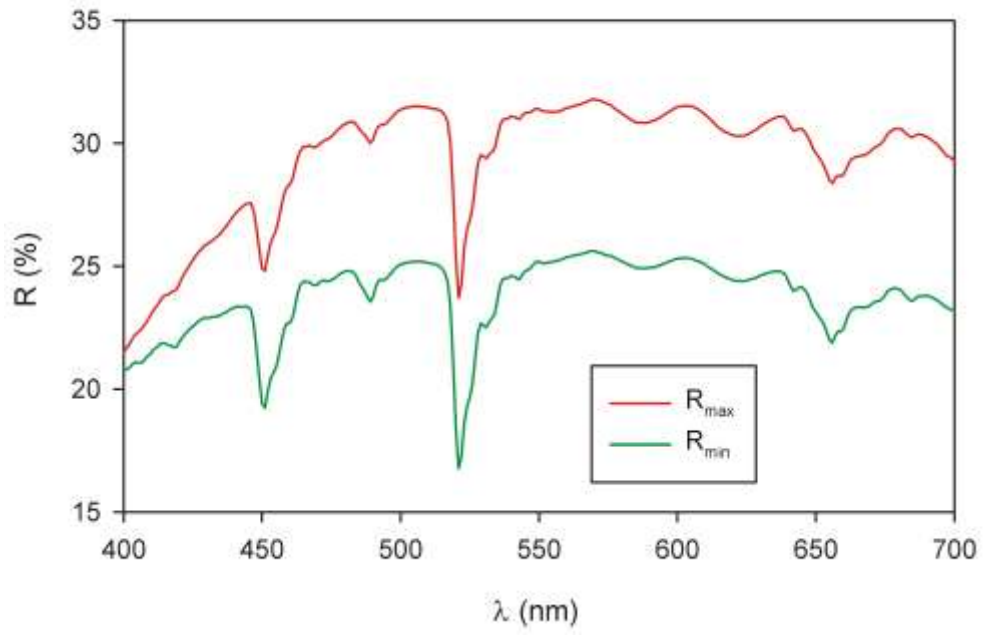
**Figure 4:** Raman spectrum of marsaalamite-(Y) (split at 2000 cm$^{-1}$).
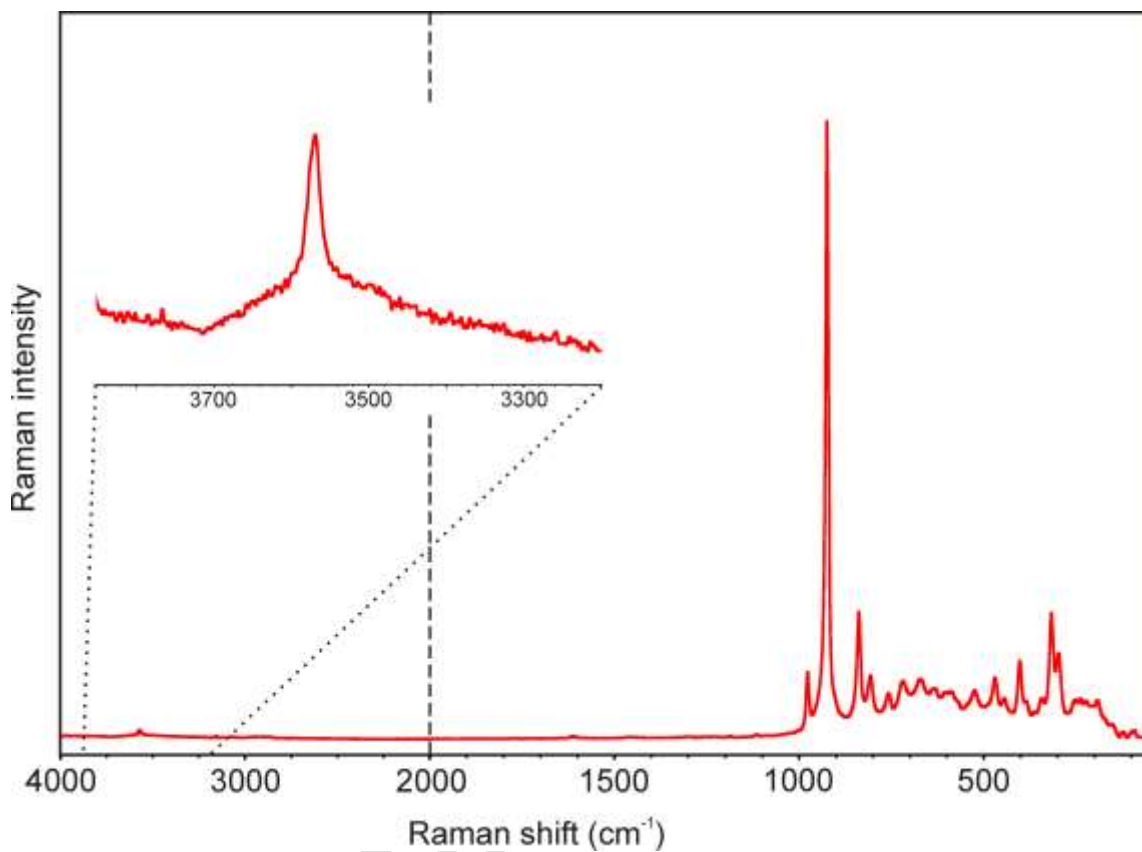
**Figure 5:** Infrared spectrum of marsaalamite-(Y) (split at 2000 cm$^{-1}$).
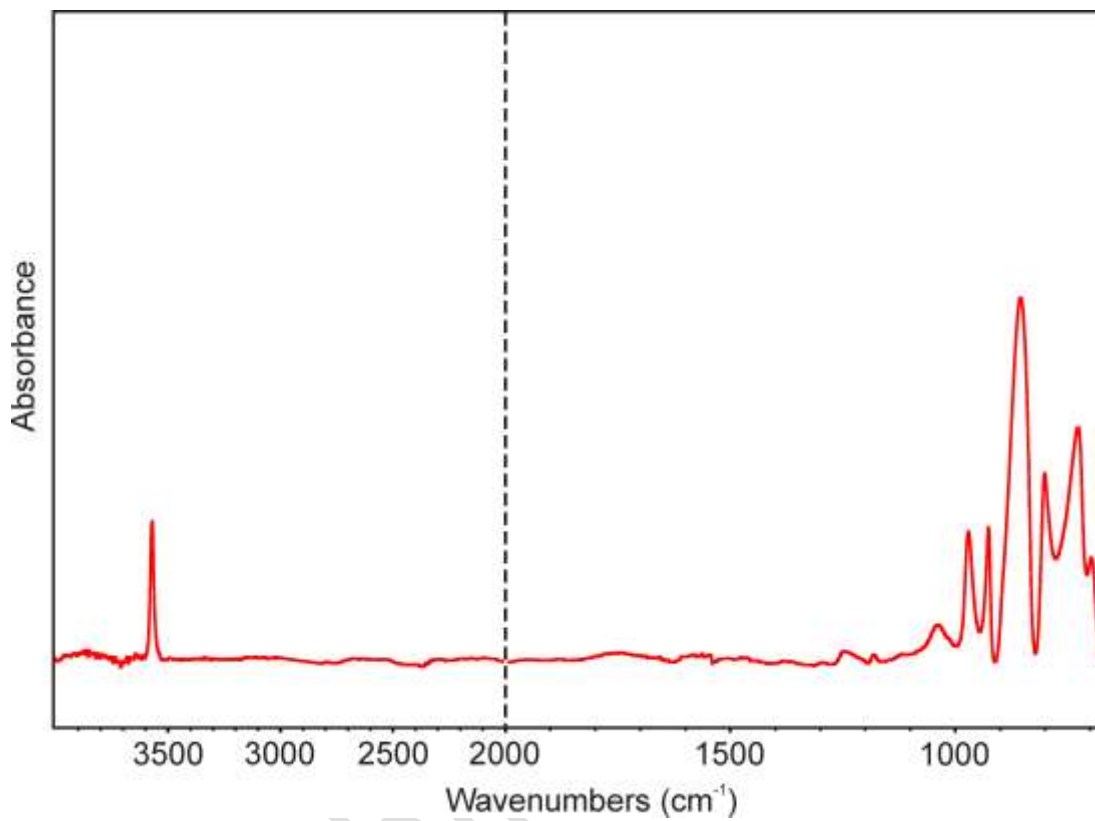
**Figure 6:** X-ray powder diffraction pattern for marsaalamite-(Y) compared to the calculated pattern of Y(MoO$_4$)F (based on the structural model of Schleid *et al.*, 2008).
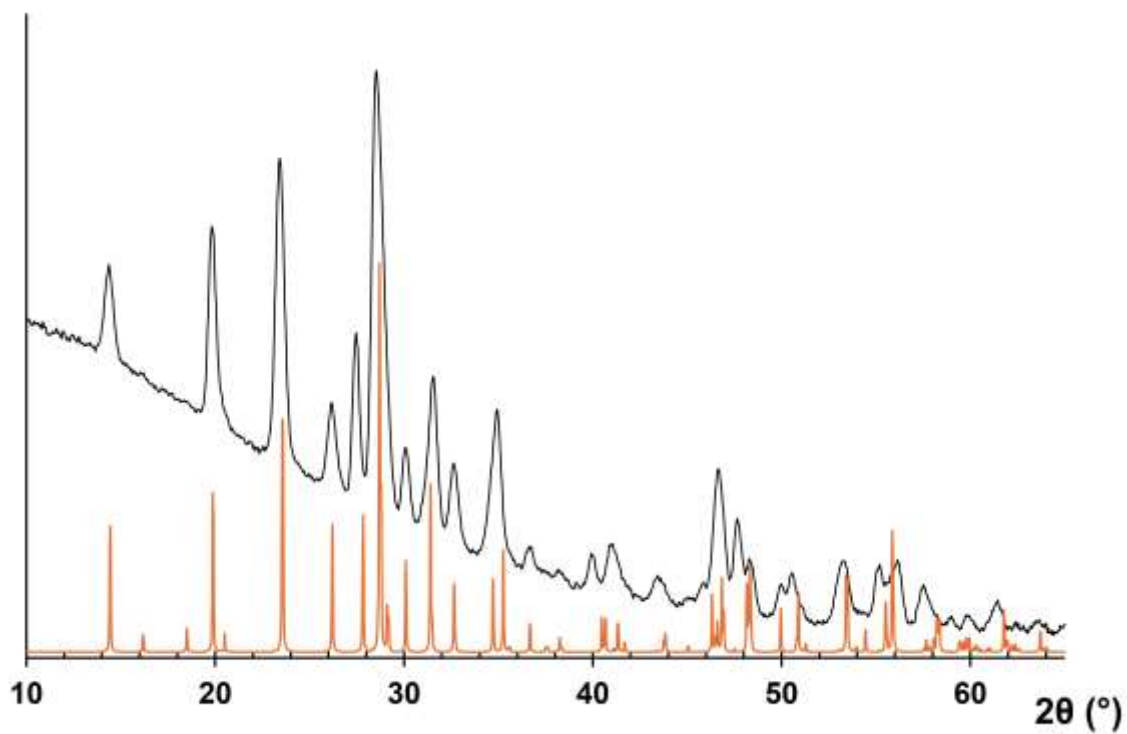
**Figure 7:** Structural model of marsaalamite-(Y), as seen down **a**, based on the structural model of synthetic $Y(MoO_4)F$ (Schleid *et al.,* 2008). Hypothetical H-bonds are shown as dashed blue lines, assuming that (OH) groups (light blue circles) occur at the same location as F atoms; Y- and Mo-centered polyhedra are shown in grey and violet, respectively, whereas red circles represent O atoms. Dashed black lines delimit the unit cell.
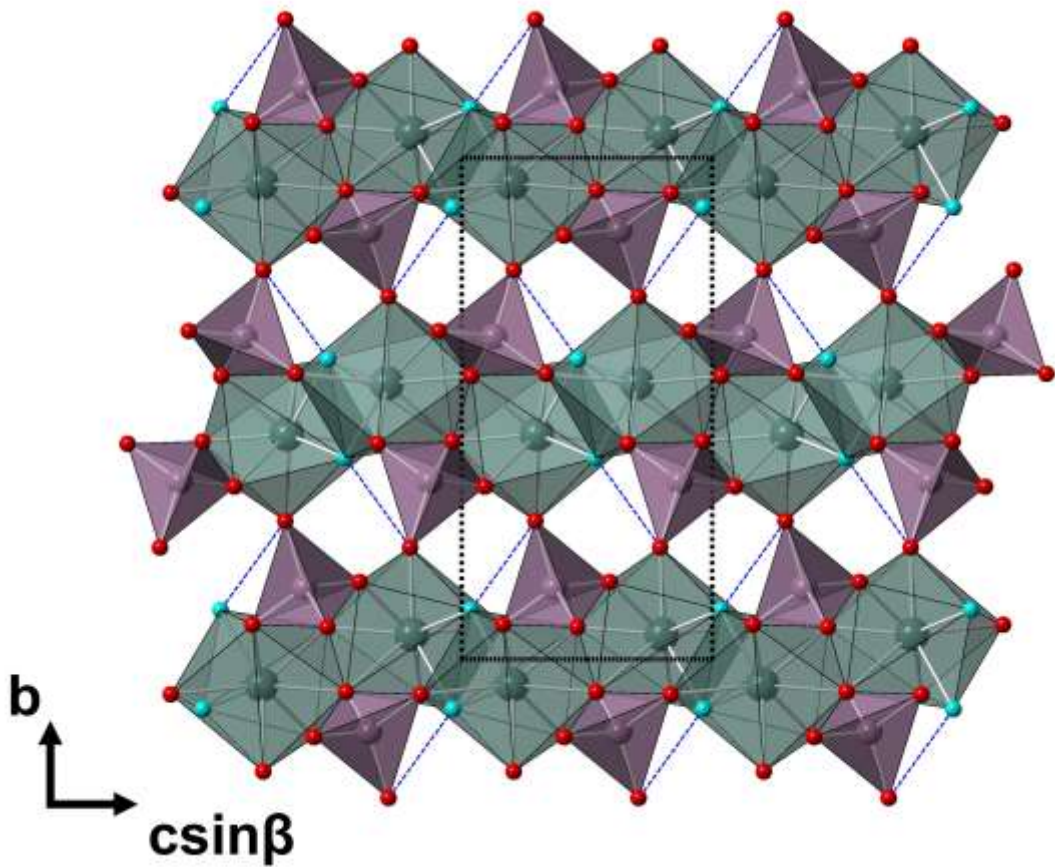
**Table 1:** Reflectance values of marsaalamite-(Y) with COM standard wavelengths given in bold

| $R_{max}$ | $R_{min}$ | $\lambda$ (nm) | $R_{max}$ | $R_{min}$ | $\lambda$ (nm) |
|---|---|---|---|---|---|
| 21.5 | 20.8 | 400 | 31.4 | 35.4 | 560 |
| 24.2 | 21.9 | 420 | 31.2 | 25.2 | 580 |
| 27.1 | 23.3 | 440 | **30.8** | **24.9** | 589 (COM) |
| 28.3 | 22.7 | 460 | 31.5 | 25.3 | 600 |
| **29.9** | **24.3** | 470 (COM) | 30.3 | 24.4 | 620 |
| 30.8 | 24.8 | 480 | 30.9 | 24.4 | 640 |
| 31.4 | 25.1 | 500 | **29.6** | **23.1** | 650 (COM) |
| 25.3 | 18.3 | 520 | 28.7 | 22.5 | 660 |
| 31.1 | 24.6 | 540 | 30.6 | 24.1 | 680 |
| **31.2** | **24.8** | 546 (COM) | 29.3 | 23.2 | 700 |

**Table 2:** Conditions used for the electron microprobe analyses.

| Element | Line | Crystal | Standard | Detection limit ($3\sigma$) in ppm |
|---|---|---|---|---|
| S | K$\alpha$ | PETL | baryte | 145-170 |
| Mo | L$\alpha$ | PETL | wulfenite | 335-360 |
| P | K$\alpha$ | PETL | apatite | 225-245 |
| As | L$\beta$ | TAP | GaAs | 1405-2010 |
| Ti | K$\alpha$ | LIF | rutile | 710-870 |
| Si | K$\alpha$ | TAP | diopside | 255-395 |
| Th | M$\alpha$ | PETL | thorianite | 270-300 |
| U | M$\beta$ | PETL | $UO_2$ | 400-420 |
| Al | K$\alpha$ | TAP | albite | 320-400 |
| Y | L$\alpha$ | PETL | $YPO_4$ | 330-390 |
| La | L$\alpha$ | LIFH | $LaPO_4$ | 435-460 |
| Ce | L$\alpha$ | LIFH | $CePO_4$ | 370-405 |
| Pr | L$\beta$ | LIFH | $PrPO_4$ | 705-740 |
| Nd | L$\alpha$ | LIFH | $NdPO_4$ | 355-380 |
| Sm | L$\beta$ | LIFH | $SmPO_4$ | 765-830 |
| Eu | L$\alpha$ | LIFH | $EuPO_4$ | 380-405 |

| Element | Line | Crystal | Standard | Range |
|---|---|---|---|---|
| Gd | Lα | LIFH | GdPO$_4$ | 425-445 |
| Tb | Lα | LIFH | TbPO$_4$ | 430-480 |
| Dy | Lα | LIFH | DyPO$_4$ | 450-490 |
| Ho | Lβ | LIFH | HoPO$_4$ | 1010-1110 |
| Er | Lα | LIFH | ErPO$_4$ | 485-535 |
| Tm | Lα | LIFH | TmPO$_4$ | 520-570 |
| Yb | Lα | LIFH | YbPO$_4$ | 550-610 |
| Lu | Lα | LIFH | LuPO$_4$ | 585-640 |
| Fe | Kα | LIF | hematite | 530-645 |
| Mn | Kα | LIF | rhodonite | 515-580 |
| Ca | Kα | PETL | diopside | 95-110 |
| Ba | Lα | LIF | baryte | 1495-1910 |
| Cl | Kα | PETL | tugtupite | 50-55 |
| F | Kα | LDE1 | fluorite | 345-370 |

**Table 3: Chemical composition and formula of marsaalamite-(Y)**

| Analyses/ wt.% (oxides) | NGH-S1 | NGH-S2 | NGH-S3 | NGH-S6 | NGH-S7 | NGH-S8 | NGH-S8 | NGH-S11 | NGH-S12 | NGH-S15 | NGH-S17 | NGH-S18 | NGH-S19 | NGH-S21 | NGH-S22 | Average |
|---|---|---|---|---|---|---|---|---|---|---|---|---|---|---|---|---|
| SO$_3$ | 0.85 | 0.84 | 0.88 | 0.89 | 0.84 | 0.85 | 0.84 | 0.90 | 0.79 | 0.82 | 0.86 | 0.82 | 0.85 | 0.86 | 0.83 | *0.85* |
| MoO$_3$ | 47.52 | 47.38 | 46.98 | 48.38 | 46.94 | 48.49 | 46.69 | 47.13 | 47.67 | 46.47 | 46.62 | 48.25 | 47.96 | 47.12 | 48.08 | *47.45* |
| P$_2$O$_5$ | 0.22 | 0.29 | 0.24 | 0.20 | 0.23 | 0.20 | 0.26 | 0.16 | 0.23 | 0.21 | 0.28 | 0.26 | 0.24 | 0.22 | 0.23 | *0.23* |
| As$_2$O$_5$ | 0.43 | 0.24 | 0.12 | 0.00 | 0.04 | 0.10 | 0.16 | 1.41 | 0.30 | 1.28 | 1.06 | 0.35 | 0.39 | 0.11 | 0.00 | *0.40* |
| SiO$_2$ | 0.13 | 0.00 | 0.06 | 0.03 | 0.00 | 0.00 | 0.01 | 0.16 | 0.00 | 0.00 | 0.91 | 0.00 | 0.09 | 0.06 | 0.06 | *0.10* |
| ThO$_2$ | 0.25 | 0.11 | 0.14 | 0.23 | 0.21 | 0.13 | 0.33 | 0.19 | 0.16 | 0.20 | 0.29 | 0.20 | 0.10 | 0.14 | 0.17 | *0.19* |
| Y$_2$O$_3$ | 26.39 | 26.54 | 26.12 | 26.69 | 26.17 | 26.93 | 26.49 | 25.82 | 26.55 | 25.91 | 25.85 | 25.78 | 26.37 | 26.05 | 26.08 | *26.25* |
| Gd$_2$O$_3$ | 0.30 | 0.25 | 0.26 | 0.21 | 0.19 | 0.21 | 0.26 | 0.30 | 0.28 | 0.28 | 0.29 | 0.23 | 0.17 | 0.28 | 0.23 | *0.25* |

26

| | 1 | 2 | 3 | 4 | 5 | 6 | 7 | 8 | 9 | 10 | 11 | 12 | 13 | 14 | 15 | 16 |
|---|---|---|---|---|---|---|---|---|---|---|---|---|---|---|---|---|
| $Tb_2O_3$ | 0.27 | 0.28 | 0.29 | 0.20 | 0.27 | 0.19 | 0.32 | 0.31 | 0.39 | 0.28 | 0.29 | 0.00 | 0.28 | 0.06 | 0.24 | *0.24* |
| $Dy_2O_3$ | 4.88 | 5.02 | 5.08 | 5.25 | 5.11 | 5.22 | 5.14 | 5.14 | 5.18 | 5.04 | 5.11 | 5.06 | 4.99 | 4.73 | 5.21 | *5.08* |
| $Ho_2O_3$ | 1.31 | 1.45 | 1.24 | 1.47 | 1.39 | 1.23 | 1.63 | 1.56 | 1.45 | 1.10 | 1.53 | 1.37 | 1.53 | 1.20 | 1.25 | *1.38* |
| $Er_2O_3$ | 6.37 | 6.64 | 6.36 | 6.47 | 6.70 | 6.48 | 6.54 | 6.55 | 6.44 | 6.20 | 6.48 | 6.77 | 6.43 | 6.52 | 6.32 | *6.48* |
| $Tm_2O_3$ | 1.12 | 1.14 | 1.01 | 1.17 | 1.03 | 1.10 | 1.12 | 0.98 | 1.12 | 0.95 | 1.08 | 1.14 | 1.14 | 1.05 | 1.19 | *1.09* |
| $Yb_2O_3$ | 5.17 | 5.54 | 5.30 | 5.43 | 5.42 | 5.43 | 5.39 | 5.42 | 5.31 | 5.17 | 5.25 | 5.43 | 5.34 | 4.99 | 5.39 | *5.33* |
| $Lu_2O_3$ | 1.01 | 1.62 | 1.55 | 1.47 | 1.47 | 1.48 | 1.56 | 0.87 | 1.43 | 0.87 | 1.40 | 1.63 | 1.56 | 0.75 | 1.50 | *1.34* |
| FeO | 0.08 | 0.06 | 0.11 | 0.01 | 0.12 | 0.04 | 0.27 | 0.03 | 0.11 | 0.30 | 0.08 | 0.04 | 0.00 | 0.07 | 0.08 | *0.09* |
| CaO | 0.10 | 0.12 | 0.12 | 0.16 | 0.15 | 0.12 | 0.15 | 0.15 | 0.15 | 0.14 | 0.14 | 0.14 | 0.18 | 0.13 | 0.14 | *0.14* |
| BaO | 0.00 | 0.36 | 0.07 | 0.17 | 0.00 | 0.00 | 0.07 | 0.00 | 0.14 | 0.00 | 0.08 | 0.06 | 0.00 | 0.15 | 0.00 | *0.07* |
| $H_2O$ calc. | 2.75 | 2.80 | 2.78 | 2.79 | 2.74 | 2.80 | 2.79 | 2.77 | 2.80 | 2.74 | 2.85 | 2.74 | 2.77 | 2.70 | 2.78 | *2.77* |
| Cl | 0.09 | 0.10 | 0.10 | 0.08 | 0.10 | 0.09 | 0.10 | 0.09 | 0.09 | 0.09 | 0.08 | 0.09 | 0.08 | 0.07 | 0.09 | *0.09* |
| F | 0.73 | 0.71 | 0.63 | 0.77 | 0.72 | 0.73 | 0.69 | 0.76 | 0.71 | 0.70 | 0.69 | 0.80 | 0.77 | 0.74 | 0.69 | *0.72* |
| O=Cl | -0.02 | -0.02 | -0.02 | -0.02 | -0.02 | -0.02 | -0.02 | -0.02 | -0.02 | -0.02 | -0.02 | -0.02 | -0.02 | -0.02 | -0.02 | *-0.02* |
| O=F | -0.31 | -0.30 | -0.26 | -0.32 | -0.30 | -0.31 | -0.29 | -0.32 | -0.30 | -0.30 | -0.29 | -0.34 | -0.32 | -0.31 | -0.29 | *-0.30* |
| Total | 99.66 | 101.17 | 99.14 | 101.72 | 99.50 | 101.48 | 100.49 | 100.36 | 100.98 | 98.46 | 100.91 | 100.79 | 100.91 | 97.69 | 100.24 | *100.23* |
| Mineral formulae (apfu) based on 2 cations and F+Cl+OH=1 | | | | | | | | | | | | | | | | |
| $S^{6+}$ | 0.031 | 0.030 | 0.032 | 0.032 | 0.030 | 0.030 | 0.030 | 0.032 | 0.028 | 0.030 | 0.030 | 0.029 | 0.030 | 0.032 | 0.030 | *0.030* |
| $Mo^{6+}$ | 0.951 | 0.939 | 0.948 | 0.954 | 0.946 | 0.957 | 0.930 | 0.937 | 0.945 | 0.938 | 0.914 | 0.961 | 0.951 | 0.961 | 0.961 | *0.946* |
| $P^{5+}$ | 0.000 | 0.001 | 0.001 | 0.000 | 0.001 | 0.000 | 0.001 | 0.007 | 0.009 | 0.008 | 0.011 | 0.011 | 0.010 | 0.009 | 0.009 | *0.000* |

27

|  | | | | | | | | | | | | | | | | |
|---|---|---|---|---|---|---|---|---|---|---|---|---|---|---|---|---|
|  | 9 | 2 | 0 | 8 | 0 | 8 | 0 | | | | | | | | | 9 |
| $As^{5+}$ | 0.011 | 0.006 | 0.003 | 0.000 | 0.001 | 0.002 | 0.004 | 0.0035 | 0.0008 | 0.0032 | 0.0026 | 0.0009 | 0.0010 | 0.0003 | 0.0000 | 0.0100 |
| $Si^{4+}$ | 0.006 | 0.000 | 0.003 | 0.002 | 0.000 | 0.000 | 0.001 | 0.0008 | 0.0000 | 0.0000 | 0.0043 | 0.0000 | 0.0004 | 0.0003 | 0.0003 | 0.0005 |
| Sum *B* | *1.008* | *0.987* | *0.996* | *0.995* | *0.987* | *0.997* | *0.975* | *1.019* | *0.990* | *1.009* | *1.024* | *1.010* | *1.004* | *1.008* | *1.003* | *1.001* |
| $Th^{4+}$ | 0.003 | 0.001 | 0.001 | 0.002 | 0.002 | 0.001 | 0.004 | 0.002 | 0.002 | 0.002 | 0.003 | 0.002 | 0.001 | 0.002 | 0.002 | 0.002 |
| $Y^{3+}$ | 0.674 | 0.670 | 0.672 | 0.671 | 0.672 | 0.678 | 0.673 | 0.655 | 0.671 | 0.667 | 0.646 | 0.655 | 0.666 | 0.678 | 0.665 | 0.667 |
| $Gd^{3+}$ | 0.005 | 0.004 | 0.004 | 0.003 | 0.003 | 0.003 | 0.004 | 0.005 | 0.004 | 0.004 | 0.005 | 0.004 | 0.003 | 0.005 | 0.004 | 0.004 |
| $Tb^{3+}$ | 0.004 | 0.004 | 0.005 | 0.003 | 0.004 | 0.003 | 0.005 | 0.005 | 0.006 | 0.005 | 0.004 | 0.000 | 0.004 | 0.001 | 0.004 | 0.004 |
| $Dy^{3+}$ | 0.075 | 0.077 | 0.079 | 0.080 | 0.079 | 0.080 | 0.079 | 0.079 | 0.079 | 0.078 | 0.077 | 0.078 | 0.076 | 0.074 | 0.080 | 0.078 |
| $Ho^{3+}$ | 0.020 | 0.022 | 0.019 | 0.022 | 0.021 | 0.019 | 0.025 | 0.024 | 0.022 | 0.017 | 0.023 | 0.021 | 0.023 | 0.019 | 0.019 | 0.021 |
| $Er^{3+}$ | 0.096 | 0.099 | 0.096 | 0.096 | 0.102 | 0.096 | 0.098 | 0.098 | 0.096 | 0.094 | 0.096 | 0.101 | 0.096 | 0.100 | 0.095 | 0.097 |
| $Tm^{3+}$ | 0.017 | 0.017 | 0.015 | 0.017 | 0.015 | 0.016 | 0.017 | 0.015 | 0.017 | 0.014 | 0.016 | 0.017 | 0.017 | 0.016 | 0.018 | 0.016 |
| $Yb^{3+}$ | 0.076 | 0.080 | 0.078 | 0.078 | 0.080 | 0.078 | 0.078 | 0.079 | 0.077 | 0.076 | 0.075 | 0.079 | 0.077 | 0.074 | 0.079 | 0.078 |
| $Lu^{3+}$ | 0.015 | 0.023 | 0.023 | 0.021 | 0.021 | 0.021 | 0.023 | 0.013 | 0.020 | 0.013 | 0.020 | 0.024 | 0.022 | 0.011 | 0.022 | 0.019 |
| $Fe^{2+}$ | 0.003 | 0.002 | 0.004 | 0.001 | 0.005 | 0.002 | 0.011 | 0.001 | 0.005 | 0.012 | 0.003 | 0.002 | 0.000 | 0.003 | 0.003 | 0.004 |
| $Ca^{2+}$ | 0.005 | 0.006 | 0.006 | 0.008 | 0.008 | 0.006 | 0.007 | 0.008 | 0.008 | 0.007 | 0.007 | 0.007 | 0.009 | 0.007 | 0.007 | 0.007 |

| | | | | | | | | | | | | | | | | |
|---|---|---|---|---|---|---|---|---|---|---|---|---|---|---|---|---|
| $Ba^{2+}$ | 0.000 | 0.007 | 0.001 | 0.003 | 0.000 | 0.000 | 0.001 | 0.000 | 0.003 | 0.000 | 0.001 | 0.001 | 0.000 | 0.003 | 0.000 | 0.001 |
| Sum $A$ | 0.992 | 1.013 | 1.004 | 1.005 | 1.013 | 1.003 | 1.025 | 0.981 | 1.010 | 0.991 | 0.976 | 0.990 | 0.996 | 0.992 | 0.997 | 0.999 |
| Cl | 0.008 | 0.008 | 0.008 | 0.007 | 0.008 | 0.007 | 0.008 | 0.007 | 0.007 | 0.008 | 0.007 | 0.007 | 0.007 | 0.006 | 0.008 | 0.007 |
| F | 0.111 | 0.107 | 0.096 | 0.114 | 0.109 | 0.109 | 0.105 | 0.114 | 0.107 | 0.107 | 0.102 | 0.121 | 0.115 | 0.114 | 0.104 | 0.109 |
| OH | 0.881 | 0.885 | 0.896 | 0.879 | 0.883 | 0.884 | 0.887 | 0.879 | 0.886 | 0.885 | 0.891 | 0.872 | 0.878 | 0.880 | 0.888 | 0.884 |
| Sum $X$ | 1.000 | 1.000 | 1.000 | 1.000 | 1.000 | 1.000 | 1.000 | 1.000 | 1.000 | 1.000 | 1.000 | 1.000 | 1.000 | 1.000 | 1.000 | 1.000 |

**Table 4:** X–ray powder diffraction data ($d$ in Å) for marsaalamite-(Y).

| $h$ | $k$ | $l$ | $d_{meas}$ | $I_{meas}$ | $d_{calc}$* | $I_{calc}$* |
|---|---|---|---|---|---|---|
| 0 | 2 | 0 | 6.162 | 22 | 6.16 | 8 |
| **1** | **1** | **1** | **4.465** | **45** | **4.485** | **20** |
| **1** | **2** | **1** | **3.793** | **70** | **3.794** | **31** |
| 0 | 3 | 1 | 3.401 | 19 | 3.408 | 17 |
| **1** | **0** | **2** | **3.248** | **38** | **3.241** | **27** |
| **1** | **1** | **2** | **3.126** | **100** | **3.134** | **100** |
| 0 | 1 | 2 | 2.97 | 16 | 2.964 | 22 |
| **1** | **-2** | **-1** | **2.839** | **35** | **2.815** | **31** |
| 0 | 2 | 2 | 2.735 | 17 | 2.736 | 28 |
| **1** | **4** | **0** | **2.57** | **34** | **2.581** | **21** |
| 0 | 3 | 2 | 2.446 | 6 | 2.451 | 15 |
| 2 | 1 | 2 | 2.354 | 3 | 2.363 | 6 |
| 2 | 2 | 2 | 2.257 | 8 | 2.242 | 17 |
| 1 | 1 | 3 | 2.194 | 11 | 2.195 | 14 |
| 2 | 3 | 2 | 2.078 | 5 | 2.077 | 18 |

| 2 | 1 | 3 | 1.978 | 6 | 1.975 | 28 |
|---|---|---|---|---|---|---|
| **0** | **6** | **1** | **1.945** | **32** | **1.946** | **19** |
| 2 | 2 | 3 | 1.906 | 22 | 1.903 | 21 |
| 1 | 6 | 1 | 1.885 | 13 | 1.889 | 32 |
| 0 | 3 | 3 | 1.824 | 8 | 1.824 | 19 |
| 1 | 4 | 3 | 1.805 | 11 | 1.807 | 19 |
| 3 | 0 | 2 | 1.719 | 14 | 1.717 | 12 |
| 1 | 0 | 4 | 1.666 | 12 | 1.666 | 23 |
| 3 | 2 | 1 | 1.637 | 15 | 1.644 | 66 |
| 3 | 1 | 3 | 1.598 | 8 | 1.592 | 36 |
| 2 | 2 | 4 | 1.567 | 3 | 1.567 | 18 |
| 1 | 3 | 4 | 1.543 | 3 | 1.544 | 22 |
| 2 | 3 | 4 | 1.51 | 6 | 1.507 | 21 |
| 1 | 8 | 0 | 1.461 | 3 | 1.464 | 59 |

Given in bold refers to the intensities of the
seven (7) strongest lines.
*Calculated $d$ and $I$ values were obtained from Le Bail fitting of measured
powder XRD pattern in the $P2_1/c$ space group.

**Table 5:** Comparison of the unit-cell parameters of marsaalamite-(Y) to
synthetic Y(MoO$_4$)F and Y(MoO$_4$)Cl (Schleid *et al.*, 2008),
and tancaite-(Ce) (Bonaccorsi and Orlandi, 2020).

| | Marsaalamite-(Y) | Y(MoO$_4$)F | Y(MoO$_4$)Cl | Tancaite-(Ce) |
|---|---|---|---|---|
| Space group | $P2_1/c$ | $P2_1/c$ | $C2/m$ | $Pm3m$ |
| $a$ [Å] | 5.1863(7) | 5.1962(2) | 10.1902(5) | 6.870(1) |
| $b$ [Å] | 12.3203(11) | 12.2514(7) | 7.2067(4) | 6.870(1) |
| $c$ [Å] | 6.6953(7) | 6.6330(3) | 6.8150(3) | 6.870(1) |
| $\beta$ [°] | 114.173(8) | 112.851(4) | 107.130(4) | 90 |
| $V$ [Å$^3$] | 390.30(8) | 389.12 | 478.28 | 324.2(1) |
| $Z$ | 4 | 4 | 4 | 1 |
| *Calculated density [g.cm–3]* | 4.900 | 4.572 | 3.948 | 3.738 |